ARTICLE   OPEN

Check for updates

Liquid-metal micro-networks with strain-induced conductivity for soft electronics and robotic skin

Yeongmin Park[1,5], Jaewoong Jung[1,5], Younghoon Lee[2], Dongwoo Lee[3], Joost J. Vlassak[4] and Yong-Lae Park [1 ✉]

Thin-film devices made of room-temperature liquid metals (LMs) have contributed to the development of electronic skin for human-robot/machine interfaces but still have limitations, including degradations of performance and robustness under repeated deformations. In this paper, we describe an interesting phenomenon of the formation of LM microscale networks (LMMNs) and propose to use the LMMNs for fabricating thin-film conductors. A simple layer-by-layer (LBL) deposition process enables the growth of a hierarchical structure of LM microdroplets that forms a conductive network (i.e., LMMN) when stretched. The strain-history behavior of LMMNs allows conductivity enhancement up to 2.37×10^6 S m^{-1} in response to increased tensile strains. By adjusting the number of LM layers in LBL deposition, the gauge factor ($0.2 \leq GF \leq 1$), the linearity, and the sheet resistance of LMMN films can be easily controlled, providing high potentials in various applications, including skin-mountable circuits, energy harvesters, and soft artificial skin.

INTRODUCTION

The role of wearable technologies is pivotal in emerging fields, such as personal healthcare1[1–4], soft robotics[5–8], and human-activity monitoring[9–13]. These areas require devices that delicately interface the human body with the environment and provide useful information to the wearer. However, the performance of current wearable devices is limited by rigid electrical components, and the discrepancy of the mechanical properties between the device and the soft human tissue induces dislocation of the devices and inaccurate data acquisition[14,15]. In this regard, researchers have developed soft and stretchable electronic materials that easily conform to three-dimensional (3D), nonuniform surfaces of the human body while maintaining their functionalities[16–18]. In particular, research efforts have been devoted to configuring these materials into ultrathin, lightweight, and skin-attachable architectures[19]. These skin-like devices are expected to provide seamless and long-term operation without causing any discomfort to the user.

One main approach to soft and stretchable electronics is to impart elasticity to intrinsically rigid conductors. A top-down strategy for this approach is to pattern thin metal films into geometric structures that dissipate strain throughout the traces. These structures employ wavy[20], serpentine[21], wrinkled[22], or intentionally fractured[23] designs that induce negligible strain to the material itself by deforming out of plane under large deformation. As the fabrication techniques for these structures usually involve conventional materials and procedures, devices made with this approach are compatible with existing electrical components. This advantage has been successfully demonstrated for skin-inspired devices that are physically imperceptible to the wearer[24,25]. Still, issues, such as low device density, stretchability only in prescribed directions, and low mechanical stability, have not been resolved. A bottom-up strategy is to embed rigid conductive particles into elastomers. These composites benefit from the large stretchability of the elastomeric matrix material, while the electrical conductivity is maintained by the percolation network of the conductive fillers[26]. Facile printing methods, including inkjet printing[27], screen printing[28], and electrohydrodynamic (EHD) printing[29], of the composite inks have been offered for fabrication of skin-like devices. These methods enabled large-scale and low-cost fabrication of devices, such as stretchable transistor arrays[30], stretchable optoelectronic devices[31–33], wearable sensors[34], and energy harvesters[35]. These nanocomposites could be designed to have high sensitivities by controlling the compositions and the structures of their conductive networks. Nevertheless, their high gauge factors and relatively low electrical conductivities hamper their applications in power transmission.

In order to overcome the above issues that stem from the inherent rigidity of conventional electrical conductors, liquid-phase conductors have been investigated. Room-temperature liquid metals (LMs), such as eutectic gallium-indium (EGaIn) or gallium–indium–tin (Galinstan), are the most appealing candidates for intrinsically stretchable conductors, since they have the best combination of electrical conductivity and stretchability[36]. Nevertheless, the rheological properties of LMs—low viscosity, high surface tension, and spontaneous formation of oxide skins[37]—hinder the use of conventional fabrication techniques. Microchannel-injection[38–40] and direct-writing/printing[41,42] methods have been proposed for patterning LMs by utilizing the fluidity. These methods enabled fabrication of various electrical components, including soft sensors, stretchable circuits, and microheaters, but required thick elastomer layers for encapsulation to prevent leakage of the liquid alloys. Patterning LMs into thin films further requires dealing with their wetting property, which is governed by the native oxide skins of gallium[43,44]. The wettability of LMs could be enhanced by controlling the surface texture of the substrate[45,46] or spreading over a solid metal film[47–49]. Several studies have reported successful fabrication of

[1]Department of Mechanical Engineering; Institute of Advanced Machines and Design; Institute of Engineering Research, Seoul National University, Seoul 08826, Korea. [2]Department of Electrical Engineering and Computer Science, Massachusetts Institute of Technology (MIT), Cambridge, MA 02139, USA. [3]School of Mechanical Engineering, Sungkyunkwan University, Suwon 16419, Korea. [4]John A. Paulson School of Engineering and Applied Sciences, Harvard University, Cambridge, MA 02138, USA. [5]These authors contributed equally: Yeongmin Park, Jaewoong Jung. ✉email: ylpark@snu.ac.kr
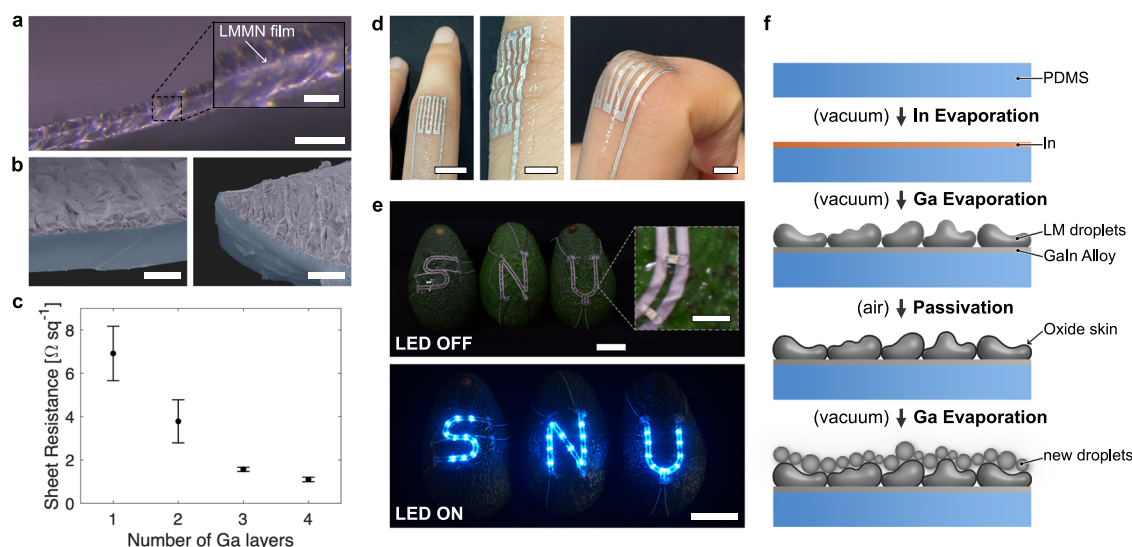
Fig. 1 LMMN films prepared with the LBL deposition method. a A cross-sectional optical micrograph of an LMMN film embedded inside a PDMS substrate with 50 μm thickness (scale bar: 100 μm; inset image scale bar: 30 μm). **b** False-color scanning electron microscopy (SEM) images of LMMN films on an ultrathin PDMS substrate (scale bars: 25 μm). Blue indicates the PDMS substrate, and violet indicates LMMN films. **c** Sheet resistances of LMMN films with different numbers of LBL-deposited gallium layers. The thickness of each layer was fixed, and the total thickness of the film varies depending on the number of gallium layers. Data were measured from $1 \times$ LBL to $4 \times$ LBL ($n = 4$ samples, error bars: standard deviation.). **d** Photographs of a resistive finger flexion sensor attached to a finger: Top view (scale bar: 10 mm), side view (scale bar: 5 mm), and under proximal interphalangeal (PIP) joint flexion (scale bar: 5 mm) from left to right. **e** Photographs of LED-embedded circuit boards patterned in "S," "N," and "U" shapes (scale bars: 3 cm; inset image scale bar: 4 mm). The circuit boards are laminated onto three avocados. **f** Schematic illustration of the LBL deposition for the fabrication of LM microstructures that form LMMN films.

uniform thin films of LMs by this strategy[50–52], but the combination of conventional microfabrication and soft lithography techniques complicates the overall procedure. Alternatively, fabricating LM particle (LMP) inks and spray-printing them into a film has been proposed as a simple method to fabricate LM films[53]. Although the film is initially non-conductive as the LMPs are separated by their oxide skins, conductive pathways could be patterned by selectively applying mechanical force or laser to sinter the LMPs[54,55]. This LMP-based composite exhibits unique properties, such as strain-invariance and self-healing[56], while a low conductivity and unwanted activation are still remaining issues.

We introduce LM thin-film conductors composed of thermally evaporated LM microstructures that form an LM microscale network (LMMN) under mechanical deformation (Fig. 1). An LM microstructure is fabricated by layer-by-layer (LBL) deposition of gallium microdroplets on the base film of indium pre-deposited on a silicone substrate; both metals are deposited by thermal evaporation. The LM microstructure fabricated by the proposed process exhibits a high initial electrical conductivity (1.72×10^6 S m^{-1}), which could be further enhanced by the formation of a structured LMMN film when exposed to tensile strain (Fig. 1a, b). We examined the formation of the LM microstructure in the suggested deposition process to engineer an LMMN film with desirable characteristics. We evaluated the performance of the LMMN films and discovered that the sheet resistance of the LMMN films could be directly controlled by adjusting the number of the LBL-deposited gallium layers (Fig. 1c). Another benefit of the LBL deposition is that we can obtain electromechanical responses with nearly constant resistances over strain (gauge factor GF = 0.2 for $\epsilon = 50\%$) as well as responses with a high linearity (coefficient of determination, $R^2 = 0.998$; GF = 1). The LMMN films that endured tensile strains up to 80% exhibited an enhanced electrical conductivity as high as 2.37×10^6 S/m with physical robustness over 10,000 cycles of 50% strain. These features, combined with the ultrathinness (thickness of approximately 2 μm; Supplementary Fig. 1) of the LMMN films, enabled various applications as on-skin electronic devices (Fig. 1d, e). We demonstrated skin-mountable circuit boards, strain sensors, and energy

harvesters to present the potential of the proposed LMMN films as stretchable thin-film artificial skin.

RESULTS

Formation of multilayered LM microstructures using LBL deposition

Thermal evaporation of EGaIn has been suggested as a method of fabricating LM nanoparticles (NPs)[57,58]. Instead of forming a thin film, the evaporated LM forms a layer of LM nanoparticles with uniform distribution due to the high surface tension. The deposited LM nanoparticles are separated individually after the deposition as thin oxide skins spontaneously form under ambient conditions. While these oxide skins play a significant role in maintaining a stable nanostructure of the LM nanoparticle layer, they prevent the conductive pathways between the particles, making it difficult to use the LM layers as an electrical device[58].

Here, we propose an alternative LBL deposition method for fabricating an LM thin-film structure with a relatively high electrical conductivity (Fig. 1f). Instead of evaporating an alloy of indium and gallium, we evaporate the two metals separately and allow them to alloy on the substrate. Indium is evaporated first on a polydimethylsiloxane (PDMS) substrate to form a solid thin film that provides an initial conductive pathway and adhesion to the substrate. We set the thickness of the indium layer to 150 nm at which a stable electrical performance was achieved over repeated strain cycles when the thickness was increased from 25 nm (Supplementary Fig. 2). Gallium is then evaporated onto the prepared indium film layer-by-layer. Although the indium layer enables the wetting of gallium, forming a liquid alloy with it, the gallium–indium alloy condenses in a dropwise fashion due to the high surface tension. After depositing a uniform layer of gallium microdroplets, we passivate them by exposing them to an atmospheric condition (Supplementary Fig. 3). The passivation seals the deposited gallium droplets with a surface oxide on which new gallium droplets can grow during subsequent gallium deposition (Supplementary Fig. 4). Excessive gallium droplets still
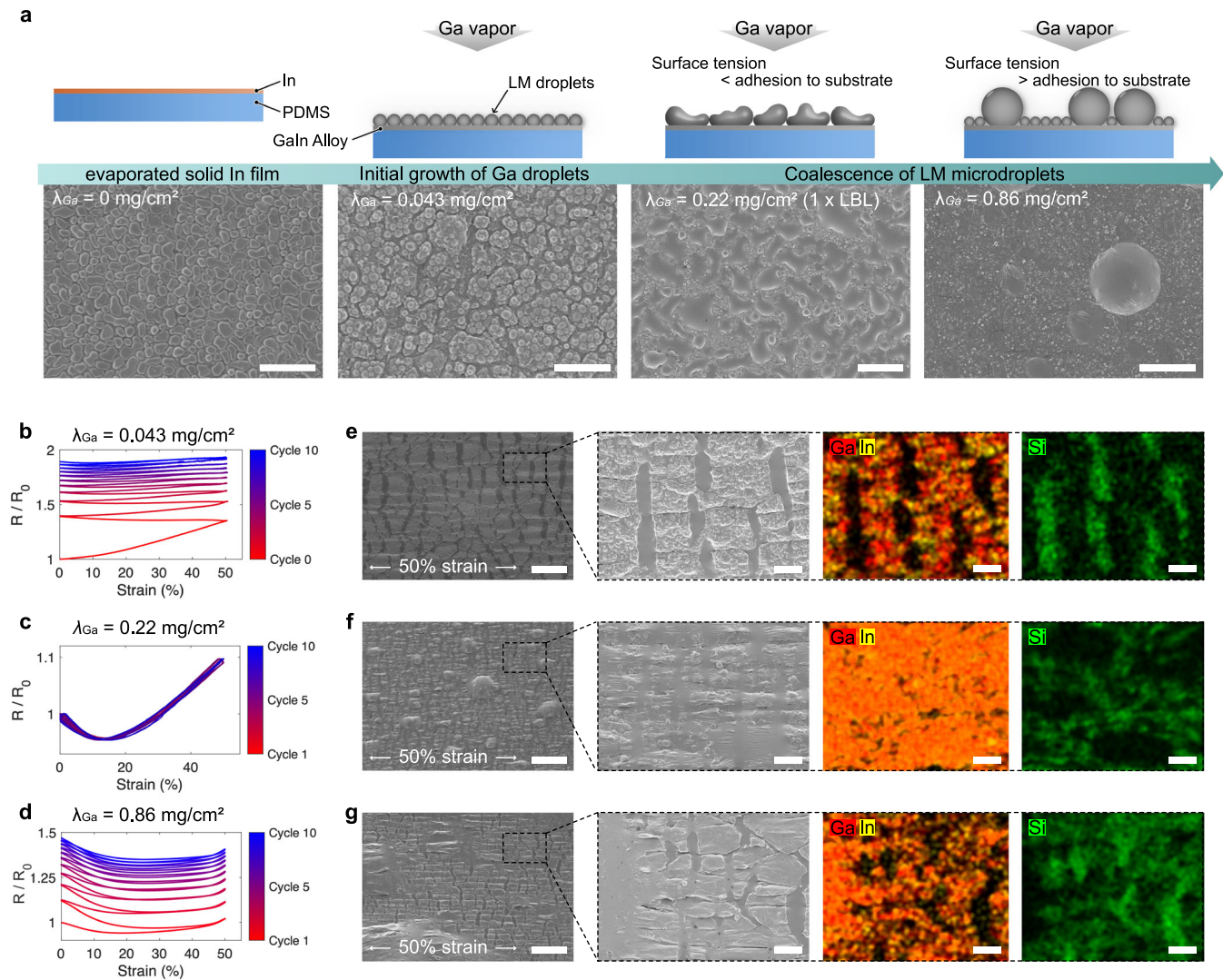
a

b $\lambda_{Ga} = 0.043$ mg/cm²

c $\lambda_{Ga} = 0.22$ mg/cm²

d $\lambda_{Ga} = 0.86$ mg/cm²

e

f

g

Fig. 2 Characterization of LM microstructures with a single gallium layer. a Evolution of an LM microstructure as the evaporated mass of gallium increases. Schematic illustrations and SEM images are presented for deposited gallium mass per unit area: $\lambda_{Ga} = 0$ mg cm^{-2}, $\lambda_{Ga} = 0.043$ mg cm^{-2}, $\lambda_{Ga} = 0.22$ mg cm^{-2}, and $\lambda_{Ga} = 0.86$ mg cm^{-2} from left to right (scale bars: 2, 2, 5, and 20 µm from left to right). An indium layer with a thickness of 150 nm was deposited onto a PDMS substrate prior to the gallium evaporation. A uniform, entire coverage of gallium on the film is achieved only with $\lambda_{Ga} = 0.22$ mg cm^{-2} (1 × LBL). **b–d** Relative resistance responses of the LM microstructures of $\lambda_{Ga} = 0.043$ mg cm^{-2} (**b**), $\lambda_{Ga} = 0.22$ mg cm^{-2} (**c**), $\lambda_{Ga} = 0.86$ mg cm^{-2} (**d**). Resistance values were measured during ten cycles of 50% tensile strain with the samples pre-strained up to 50% before the measurement. **e–g** SEM images and energy dispersive spectroscopy (EDS) mappings of the LM microstructures of $\lambda_{Ga} = 0.043$ mg cm^{-2} (**e**), $\lambda_{Ga} = 0.22$ mg cm^{-2} (**f**), $\lambda_{Ga} = 0.86$ mg cm^{-2} (**g**) under 50% tensile strain; gallium (red) and indium (yellow) are the evaporated metals; silicon (green) represents the underlying PDMS substrate (scale bars: 10 µm; inset image scale bars: 2 µm).

remain liquid as a result of supercooling[59]. The LBL deposition—piling up uniform layers of LM microdroplets by repeating the deposition and passivation sequence—is thereby enabled. The proposed LBL process has two main contributions compared with the existing work[57,58]. First, the indium layer not only creates the initial conductive pathways of the film even with the oxide skins in the individual gallium droplets but also provides a bonding layer for gallium, enabling rupture of the gallium droplets with strain for the formation of conductive networks. Second, the repeated cycles of deposition and passivation allow for stable deposition of multiple thin gallium layers separated by oxide skins, enabling controllability of the film characteristics, such as sheet resistance and gauge factor.

A stable LM microstructure fabricated by LBL-deposition requires each layer of gallium droplets to have a uniform distribution, and we studied the growth cycle of gallium droplets

on an indium film to determine the amount of gallium to be deposited (see Fig. 2a, Supplementary Note 1, and Supplementary Figs. 5 to 7). The initial nucleation of gallium occurs uniformly across the film and is rapidly followed by coalescence between adjacent droplets. Instead of re-exposing areas of the underlying indium that allows the formation of new gallium droplets, the droplets merge into peanut-shaped lumps and remain attached to their original locations due to the strong adhesion between indium and gallium by alloying. The microstructure comprises these evenly distributed lumps at this stage ($\lambda_{Ga} = 0.22$ mg cm^{-2}) while subsequent nucleation is suppressed. This uniformity is maintained until the size of the lumps grows enough for their surface tension to overcome the adhesion force to the indium surface. As the lumps are detached from their initial positions during coalescence, nucleation of new droplets is facilitated. Subsequent cycles of formation of lumps deplete the solid indium

layer by repeatedly forming supercooled liquid alloys. During these cycles, the shape of the lumps becomes a hemisphere due to the high surface tension (Supplementary Figs. 8 and 9). The distribution of the lumps in the microstructure becomes inhomogeneous, with submicron-sized fresh nuclei covering most of the film while large hemispherical lumps of approximately 20 μm are sporadically distributed.

The electromechanical behavior of the LM microstructures with one gallium layer is depicted in Fig. 2b–d (see also Supplementary Fig. 10). While a microstructure with $\lambda_{Ga} = 0.22\,\text{mg}\,\text{cm}^{-2}$ showed a recoverable strain-resistance response, microstructures with $\lambda_{Ga} = 0.043\,\text{mg}\,\text{cm}^{-2}$ and $\lambda_{Ga} = 0.86\,\text{mg}\,\text{cm}^{-2}$ were not able to recover their initial resistances. This is because, for $\lambda_{Ga} = 0.043\,\text{mg}\,\text{cm}^{-2}$, the size of the LM droplets is not large enough to cover the microcracks. As for $\lambda_{Ga} = 0.86\,\text{mg}\,\text{cm}^{-2}$, despite the increased amount of the evaporated gallium, the liquid metal volume accumulates in specific locations. These accumulated LM droplets only cover microcracks around their locations and cannot prevent permanent damage to the entire film. Figure 2e to g show the scanning electron micrographs, along with energy dispersive spectroscopy (SEM-EDS) analyses under tensile strain ($\epsilon = 50\%$) in the LM microstructures. Microcracks can be observed in the regions where the signals of the metals are not detected while the silicon signals associated with the PDMS substrate are visible. The LM microstructure with $\lambda_{Ga} = 0.22\,\text{mg}\,\text{cm}^{-2}$ did not crack under the same deformation. We, therefore, define one layer of gallium droplets in the LBL deposition process as $\lambda_{Ga} = 0.22\,\text{mg}\,\text{cm}^{-2}$. An LM microstructure that has N layers of LBL deposition is denoted as $N \times$ LBL.

Transition of multilayered LM structures to LMMN films

When tensile strain is applied to a film with LBL-deposited gallium, the oxide skin of the microdroplets ruptures and causes the LM inside to leak out of the shell. This leakage results in an extensive coalescence of the LM protrusions, leading to the connection of a conductive network throughout the substrate. Figure 3a, b shows the transition of the stacked gallium microdroplets on an indium layer to a conductive pathway of the LMMN triggered by tensile strain. When the strain is released, the LMMN film goes into compression resulting in an out-of-plane deformation. This out-of-plane deformation results in the development of structures that are aligned orthogonally to the direction of the strain. These structures remain stable due to the instantaneous formation of an oxide skin on the surface of the LM. The coalescence of LM also increases an effective contact area between the underlying indium and the stacked gallium, causing intermixing of the two metal layers. X-ray diffraction (XRD) patterns of the films analyzing the impact of applying a strain are shown in Fig. 3c. The XRD patterns clearly demonstrate that the diffraction peak corresponding to solid indium is reduced after the application of strain. This observation suggests that the gallium droplets alloy with the indium to form a liquid phase that remains stable under stretching.

We next measured the resistance of the LMMN film ($3 \times$ LBL) in response to an applied strain, with ten cycles of 50% strain, as shown in Fig. 3d. A drop in the resistance occurred during the extension period of the first cycle, which was consistent with the microscopy analysis that showed the formation of the LMMN by strain. The resistance at zero strain dropped to 78% of its initial value after the application of 50% strain, indicating that mechanical strains reinforce the electrical connections of the LMMN, enhancing the conductivity of the film. During subsequent cycles, the resistance curve consistently conformed to the relaxation curve of the first cycle while maintaining its zero-strain resistance with high repeatability. This result implies that the permanent drop of the zero-strain resistance induced by the reinforcement of the electrical connections occurs when the film

experiences strain for the first time and that the zero-strain resistance is not affected by subsequent cycles of strain with the same amplitude.

The characteristics of the LBL-deposited films with various numbers of gallium layers were studied. Figure 3e shows the XRD analysis of the LBL-deposited films, where an increase in the intensity of the liquid peak is observed as more layers are deposited. This observation implies that the amount of conductive material in the film can be modulated by varying the number of gallium layers, allowing controllability of the sheet resistance, as shown in Fig. 1c.

By varying the number of the gallium layers, we can also adjust the electromechanical response of the LMMN film. Figure 3f shows the spectrum of the strain-resistance response of LMMN films with various numbers of gallium layers that had already experienced a strain cycle, showing consistent zero-strain resistances. In the case of the film with a single gallium layer ($1 \times$ LBL), a drop of electrical resistance occurred in the low strain range, followed by an increase of resistance in the high strain range. We hypothesize that this non-monotonic response stems from the surface topology of the LMMN film comprising out-of-plane LM lumps that contain the LM volume outside the conductive network (Supplementary Fig. 11). These lumps contract in the orthogonal direction of the plane of stretch when the film goes under tensile strain. As the lumps flatten, the volume of the LM that engages in the conductive network increases, resulting in a drop in resistance[60]. As applied strain continues to increase, most of the LM in the lumps contribute to the conductive network, and the resistance starts to rise due to the increased length and the decreased cross-sectional area of the conductive pathways[61].

In the case of the LMMN film with four gallium layers ($4 \times$ LBL), the electrical resistance showed a linear monotonic rise with increased tensile strain. This difference in the electromechanical response comes from the different amounts of the LM on the film surface. When the film with abundant LM experiences tensile strain, the conductive LMMN network formed by protruded LM is fully developed across the substrate at zero strain (Supplementary Fig. 12). In other words, all of the deposited LM engages in the conductive network at zero strain, resulting in the monotonic rise of electrical resistance. Another noticeable aspect was that the slope of the resistance curve of the LMMN film under strain was lower than that of bulk conductors following the Pouillet's law. Since the LMMN film consists of randomly connected conductive micro-networks, the current flow direction is not always parallel to the direction of strain. When the film is stretched, the resistance of a conductive pathway that is orthogonal to the direction of strain drops due to the increased cross-sectional area and decreased length. As a result, the strain-resistance curve of LMMN shows a lower slope than that of the bulk LM[62].

Strain-induced conductivity enhancement of LMMN films

In order to further investigate the initial formation of the LMMN when the film is subjected to strain for the first time, incremental strain sequences from 10 to 50% were applied to the film ($4 \times$ LBL) (Fig. 4a–c). The tension period of the strain sequences can be divided into two distinct phases: the 'tracing phase' and the 'reinforcing phase.' As long as the strain is smaller than the maximum strain experienced previously, the resistance curves trace the relaxation curve (plotted as dashed curves in Fig. 4c) of the previous sequence, which was also observed in the earlier result in Fig. 3d. When the applied strain exceeds the maximum strain value of the previous sequence, additional rupture of the oxide skin induces increased coalescence of LM, resulting in reinforcement of the LMMN and thus enhancing the electrical conductivity. During the relaxation period, the resistance value drops as the strain decreases, which is shown in the
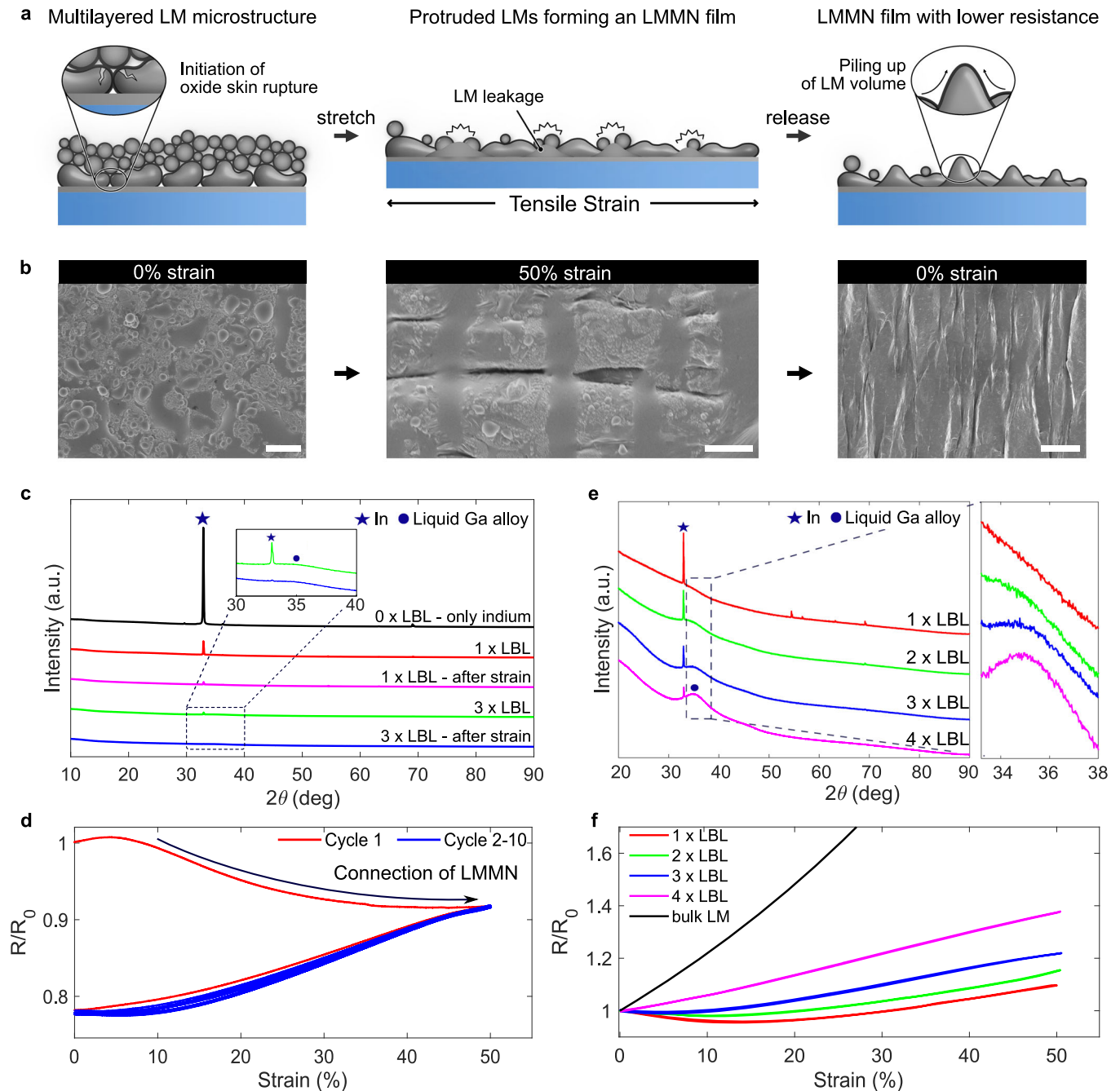
Fig. 3 Connection of LMMN. a Schematic representation of a transition of a multilayered LM microstructure to an LMMN film. **b** Corresponding SEM Images of the transition of a multilayered LM microstructure with four gallium layers (4 × LBL) before stretch (scale bar: 2 µm), stretched up to 50% strain (scale bar: 2 µm), and released from the strain (scale bar: 10 µm) from left to right. **c** XRD patterns of multilayered LM microstructures (1 × LBL and 3 × LBL) before and after strain. The sharp peak corresponding to the indium (101) plane (ICDD PDF Card 3065-929) decreases after strain experience. The wide peak around 35° corresponds to liquid gallium alloy. **d** Relative resistance response of the multilayered LM microstructure (3 × LBL) to the first ten cycles of 50% tensile strain. **e** XRD patterns of the LMMN films with different numbers of gallium layers (1–4 × LBL). Note that the films did not experience any strain. **f** Relative resistance response of LMMN films with different numbers of gallium layers (1–4 × LBL). The films experienced 50% strain before the measurement. The response of bulk LM (black curve) was calculated under the assumption of constant electrical conductivity.

strain-resistance response of the film. From the observations above, it can be concluded that exposure of an LMMN film to an increasing strain reinforces the conductive network, resulting in enhanced electrical conductivity. As a result, the electromechanical response of the film is determined by the maximum strain experienced by the film. A few studies on LM-based stretchable conductors have also shown that the electromechanical response depends on the strain history[60,63]. In these studies, the electrical

conductivity increases in response to an applied strain, but the initial state of the LM structure was nonconductive ($\sigma < 10$ S/m), which is different from LMMN films. The relation between the maximum strain applied and the volumetric electrical conductivity of the LMMN film is plotted in Fig. 4d, demonstrating a 30% rise in conductivity as the film is strained by 80%. The LMMN film that experienced 80% strain showed outstanding electrical conductivity after unloading to zero strain (2.37×10^6 S/m).
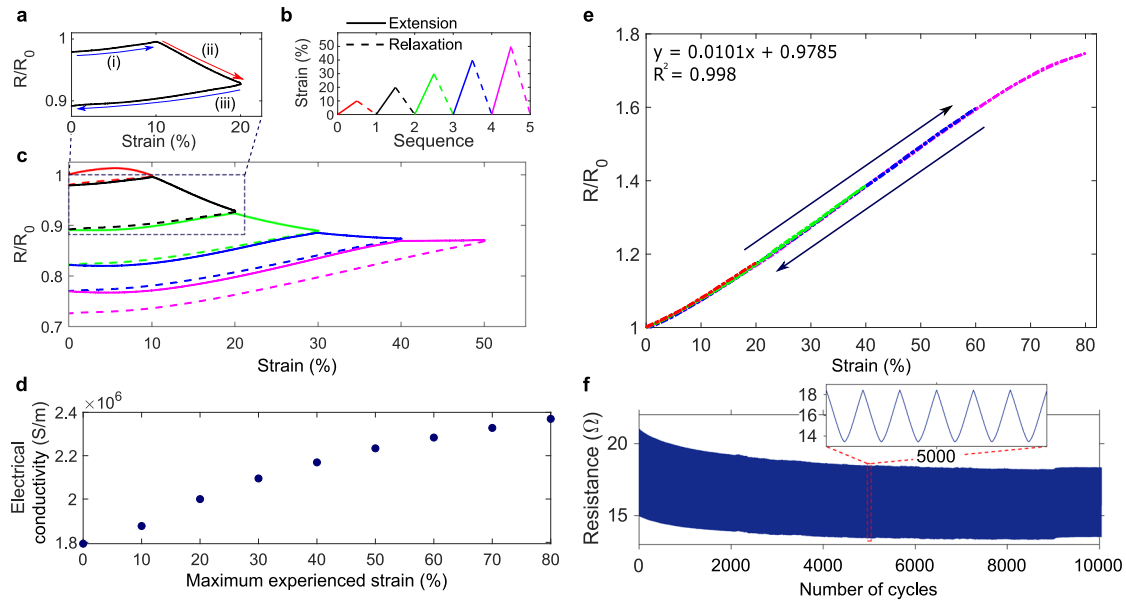
Fig. 4 Electromechanical characterization of LMMN films. a–c Relative resistance response of the LMMN film under incremental cyclic loading. **a** The second cycle sequence up to 20% strain. (i) Tracing previous curve, (ii) reinforcement of LMMN, and (iii) new strain-resistance curve. **b** Tensile strain profile, **c** the entire relative resistance response. **d** Volumetric electrical conductivity of LMMN films with different values of maximum experienced strain. **e** The relative resistance versus strain plot of the LMMN film with former strain experience up to 80%. Increasing strain sequence was applied from 20 to 80% during the measurement. **f** Resistance response of an LMMN film over 10,000 cycles to 50% strain.

Figure 4e shows the results of the electromechanical characterization of the LMMN film (4 × LBL). Since we aimed to utilize LMMN films in skin-like devices, we needed the resistance of the LMMN film to show a predictable and linear response to strain in the deformation range of human skin and joints. The strain value of human skin with wrinkles does not exceed 55%[64]. Thus, we pre-stretched the LMMN film up to 80% before its electromechanical characterization. The LMMN film was subjected to incremental strain sequences from 20 to 80% (see also Supplementary Fig. 13). Compared to recent studies on stretchable conductors, the proposed LMMN film showed a high linearity ($R^2 = 0.998$) with a low gauge factor (GF $= \Delta R/\epsilon R_0 < 1$). The strain-resistance response showed negligible hysteresis, which is a promising feature of LMMN films as a sensing component in various applications. In order to verify the physical robustness of the film, 10,000 cycles of 50% strain were applied to the film (Fig. 4f and Supplementary Fig. 14). The resistance response of the LMMN film stabilized with a slight drop in zero-strain resistance. We hypothesize that the resistance drop is due to the alignment of conductive networks as the sequence of cyclic strain progresses. As shown in Supplementary Fig. 14, repeated stretching induces the conductive network to align uniformly in the direction of strain, resulting in lowered zero-strain resistance.

Applications for skin-like devices

We demonstrate the capabilities of LMMN films for a wide range of applications for skin-like devices by illustrating several distinct examples: skin-mountable circuits, resistive strain sensors, and triboelectric nanogenerators (TENGs). These devices were fabricated to have encapsulating PDMS layers with thicknesses of approximately 25 µm for top and bottom layers each so that the overall thickness of the devices is around 50 µm. We first fabricated various stretchable and skin-mountable circuits with LMMN films and embedded microchips. Prior to the implementation, we tested various deformation modes with the LMMN film (Supplementary Figs. 15 and 16). A specimen was prepared with a circuit containing a light-emitting diode (LED), and the I–V characteristic curve was measured up to 80% tensile strain.

These results indicate that the circuit robustly operated under deformation with negligible degradation of its functionalities. We then applied cyclic tensile strain up to 50% to the circuit to demonstrate its durability. The brightness of the LED remained visibly stable throughout the cycles (Supplementary Movie 1). A thin and skin-attachable circuit was devised based on the above characterization (Fig. 5a–d and Supplementary Fig. 17). An LMMN film was patterned to be thin metal wires for delivering electrical power and signals to the microchips. A microcontroller unit (MCU) was embedded in the circuit to control three LEDs by touching the tactile sensing pad made of an LMMN film. We laminated the device directly onto a human wrist, which is a common location for attaching commercial wearable devices[65]. The device was thin and stretchable enough to allow for natural joint movements of the wrist without causing delamination of the device and discomfort to the wearer. The ability of LMMN films to maintain high conductivity enabled the stable operation of the device even under wrist deformation (Fig. 5d and Supplementary Movie 1).

Energy harvesting was readily realized by introducing tribotronics into an LMMN film embedded in PDMS without additional modifications to its structure (Fig. 5e–g and Supplementary Fig. 18)[66,67]. When the LMMN film was touched repeatedly, peak-to-peak voltages up to 120 V were generated based on triboelectrification and electrostatic induction, which are the mechanism of TENGs. Thanks to the reliable stretchability of LMMN films with low gauge factors, power generation was possible even under 50% of areal strain (Fig. 5g). Furthermore, the power generated by a gentle touch of a gloved finger was directly utilized to light up 11 LEDs connected in series (Fig. 5e, f, Supplementary Fig. 18, and Supplementary Movie 2). The generated energy could also be stored in a capacitor (Supplementary Fig. 19). Depending on the number of applied touches from 5 to 30 times on the LMMN film, the capacitor was charged from 0.8 to 5 V. This demonstration indicates that energy generated by the LMMN film can be stored and can be practically used when necessary.

We also embedded an LMMN film (4 × LBL) with a serpentine pattern in a thin PDMS substrate to be used as a strain sensor. The thin PDMS substrate was then attached to a finger joint to form a
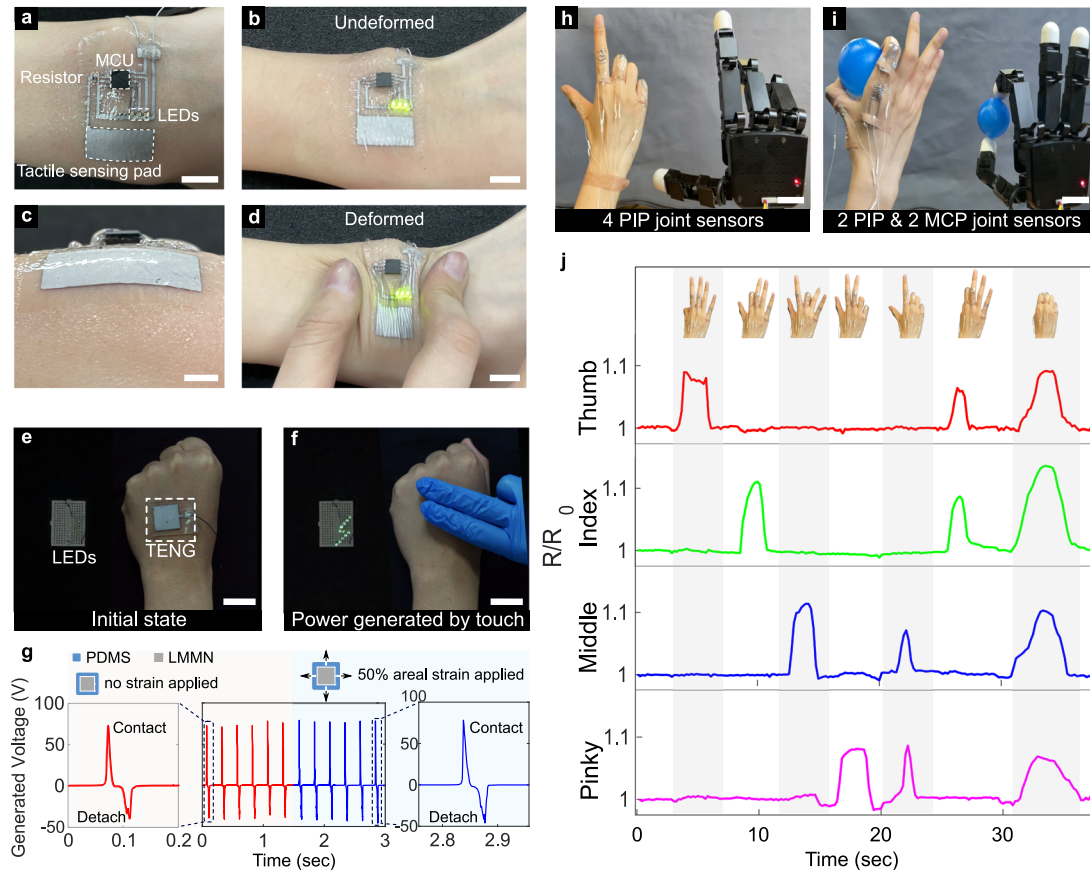
Fig. 5 Applications of LMMN films. a–d A skin-attachable circuit board patterned with LMMN films attached to a human wrist (**a**, **b**; scale bars: 1 cm). The device robustly operates without deformation (**c**; scale bar: 5 mm) and with deformation (**d**; scale bar: 1 cm). **e–g** LMMN film utilized as a triboelectric nanogenerator (TENG). **e** LMMN-TENG mounted on a human hand (scale bar: 2 cm). **f** Electrical current lighting up eleven LEDs is generated under gentle touch (scale bar: 2 cm). **g** Voltage output under zero strain (red) and when 50% of areal strain is applied to the substrate (blue). Peak-to-peak voltages up to 120 V were generated with consistency. **h–j** Finger flexion sensors for the teleoperation of a robotic hand. **h** Photograph of the demonstration with four PIP joint sensors (scale bar: 3 cm). **i** Photograph of the demonstration with two PIP joints and two metacarpophalangeal joints (MCP) joints (scale bar: 3 cm). **j** Relative resistance changes of four PIP joint sensors with different hand gestures.

skin-like device for measuring joint angles (Fig. 1d). Taking advantage of the linear strain-resistance response of the LMMN film, reliable finger joint angle data were acquired and characterized with a vision-based motion tracking system (Supplementary Fig. 20). Furthermore, teleoperation between a robotic hand and a human hand was performed to demonstrate the utility of the LMMN films (Fig. 5h, i and Supplementary Movies 3, 4). Since the electrical resistance of the LMMN film changed immediately as the film deformed, response delay of the sensor was negligible (Supplementary Fig. 21). Figure 5j shows the response of the relative resistance values (R/R_0) of the LMMN film sensors to various finger gestures.

DISCUSSION

In this paper, we presented an LM thin-film structure that exhibits a favorable electromechanical behavior suitable for a myriad of applications in stretchable skin-like devices. The LM structure is fabricated by an LBL deposition method that piles up densely packed layers of LM microdroplets. This manufacturing process only involves thermal evaporation of indium and gallium and thus enables a single chamber fabrication of an LM thin-film conductor without manual handling of the materials. Also, the proposed LBL deposition enables the fabrication of LM thin-film conductors with an adjustable electromechanical response not obtainable with bulk LMs. The LM structures fabricated by this process readily form a conductive

network, i.e., an LMMN, under tensile strain. The LMMN films showed strain-induced conductivity enhancement caused by the additional rupture of oxide skins of the LM microdroplets. By adjusting the number of layers and enhancing the conductivity with strain, we obtained a stretchable thin-film LMMN conductor with a combination of high electrical conductivity (2.37×10^6 S m^{-1}), a high linearity ($R^2 = 0.998$), and a low gauge factor (GF ≤ 1) that has not been reported in previous work. This trait of the LMMN films enables the implementation of distinctive skin-like applications, such as skin-mountable circuit boards, energy harvesters utilizing tribotronics, and resistive strain sensors for robotic teleoperation.

Despite the favorable attributes of the LMMN films we demonstrated, there are still rooms for further improvement in fabrication. First, efforts should be made to increase the patterning resolution of the LMMN films. In this study, we focused on developing a new LM thin-film conductor and characterizing them rather than proposing a high-resolution patterning method. For fabricating specimens for strain tests and various on-skin circuit elements, simple and disposable shadow masks were sufficient. However, it is necessary to improve the resolution for fabricating integrated on-skin circuits and achieving a high device density. One possible solution is to combine photolithography microfabrication techniques. Since the proposed LBL deposition method is compatible with conventional thermal evaporation processes, we expect that a standard lift-off process could be applied to LMMN films. Furthermore, the lift-off

process may prevent substrate damage induced by physically peeling off the shadow masks. We hypothesize that the best achievable resolution will be limited by the size of the LM droplets (around several microns) in each layer, which is hardly achieved by other LM patterning methods[38–42] that do not include conventional microfabrication.

Another source of future innovation is the investigation on the potential for integrated multifunctional devices. Although LMMN films showed promising features as stretchable conductors, combinations with various electronic components, such as dielectrics and semiconductors, are crucial in achieving multiple sensing capabilities and developing integrated on-skin devices. In addition to studying the interaction of the LMMN films and other materials, an integrated fabrication process that includes the LBL deposition method and the patterning of various nanomaterials and polymeric materials should be devised. Furthermore, realizing different electrical properties of LMMN films in one circuit by controlling the number of the deposited layers may open up possibilities of fabricating multifunctional devices.

In summary, our future work will mainly focus on developing an integrated skin electronic platform by implementing a high-resolution patterning method, combining various electronic materials, and realizing tunable characteristics in a single substrate. Other future plans include optimizing the amount of gallium needed in each layer of LM droplets to enhance the electrical performance of LMMN films further and the stochastic analysis on the microstructures that yield the specific electro-mechanical behaviors of the LMMN films. These efforts will provide further opportunities for fields that require multifunctional on-skin electronics, including personal healthcare, human-activity monitoring, and soft robotics.

METHODS
Materials
LMMN films were prepared by thermally evaporating indium and gallium. These metals were purchased from Taewon Scientific Co. in the form of pellets. All LMMN films were deposited on a polydimethylsiloxane substrate (Sylgard 184; 10:1 ratio of base to curing agent; Dow Corning). Poly (acrylic acid) (PAA) powder (~450 kDa, Sigma Aldrich) was dissolved in deionized (DI) water and spin-coated on a silicon wafer to provide a water-soluble sacrificial layer. The PAA solution was neutralized to pH 7.00 with a saturated NaOH solution to form a 2 wt% solution. LMMN films were connected to copper wires using silver pastes (P-100, CANS) or small drops of EGaIn. Flowable sealants (DOWSIL™ 3140 RTV Coating, Dow Corning) were used to secure the interconnects. A 1 mm-thick double-sided tape (3 M VHB 4910) and a skin-safe adhesive silicone (Skin Tite;™ Smooth-On, Inc.) were used to attach the on-skin devices to the human hand.

Preparation of Substrates
To fabricate a thin and skin-conformal elastomeric substrate, PAA was used as a water-soluble sacrificial layer. A sacrificial layer was deposited by spin-coating (2000 rpm, 30 s) this solution on a silicon wafer. Prior to the deposition of the PAA solution, the silicon wafer was treated with air plasma (vacuum under 16 Pa, 180 s, EQ-PCE-3 MTI Corp.) in order to enhance the wettability. After drying the spin-coated sacrificial layer on a hot plate (95 °C, 3 min), PDMS was spin-coated onto the sacrificial layer (2500 rpm, 60 s) and cured in a convection oven (60 °C, 12 h) to form a stretchable and thin elastomeric substrate with a thickness around 25 μm. After the deposition of the LMNN film and sealing with another layer of PDMS with the same thickness, the substrate was immersed in water for several hours until the sample and the silicon wafer were completely separated. The total thickness of the encapsulation layer is approximately 50 μm.

Fabrication of LMMN films
The LMMN films presented in this paper were fabricated by the proposed LBL deposition. A shadow mask made of polyimide (PI) tape was fabricated by a laser cutter (Speedy 300, Trotec) with a pattern designed for each application. The resolution of the laser patterning technique is presented in Supplementary Fig. 22. The PI shadow mask was attached to a PDMS substrate. After cleaning the surface of the prepared PDMS substrate with isopropyl alcohol and air plasma, the substrate was placed in the vacuum chamber of a thermal evaporator (Thermal Evaporator System, DD High-tech). Indium was deposited once to form a solid metal layer, and then gallium was LBL-deposited. The vacuum level was maintained under 1.0×10^{-3} Pa during the evaporation of the metals, and the deposition rates of indium and gallium were set at 2 Å s^{-1} and 3 Å s^{-1}, respectively. The LM microdroplets were passivated by introducing ambient air into the chamber for 60 s with air pressure over 1.0×10^3 Pa. By applying tensile strain to the resulting LM microstructure, we can obtain LMMN films with a thickness of several micrometers.

Materials characterization
The morphologies of the samples were characterized by field-emission scanning electron microscopy (FESEM) using Zeiss SUPRA 55VP, equipped with an XFlash Detector 4010 (Bruker) for energy-dispersive X-ray spectroscopy (EDS) analysis. Height mapping was performed using a Zeiss LSM 800 MAT 3D surface confocal laser scanning microscope. XRD analysis was conducted using a Rigaku SmartLab diffractometer with a Cu Kα (λ = 1.54 Å) radiation.

Electromechanical characterization
A specimen for strain test was prepared by molding a 1 mm-thick PDMS substrate on an ultra-violet (UV) cured thermoplastic (Veroblack, Stratasys) mold programmed by a 3D printer (Objet30, Stratasys) (Supplementary Fig. 23). The LMMN film pattern with 30 mm in length and 1 mm in width was LBL deposited on the PDMS substrate, followed by spin-coating the top surface with PDMS (2500 rpm, 60 s) to form a thin encapsulating layer of 25 μm. A quantificational study of a deposited mass of gallium was performed (Supplementary Fig. 7) to calculate the average thickness of the deposited gallium as $t = m/\rho A$, where A is the area of the LMMN pattern and ρ is the density of gallium. Based on the calculated thickness of the LMMN film, its electrical conductivity was calculated as $\sigma = l/Rwt$, where R, l, w, t stands for electrical resistance, length, width, and the thickness of the LMMN pattern, respectively. Samples were clamped on a motorized test stand (ESM303, Mark-10) and were stretched up to various strain values with a rate of 60 mm/min. The electrical resistance of the LMNN film was measured by a voltage divider circuit and an analog-to-digital converter (ADC) (ADS1115, Texas Instruments) via an I^{2}C communication protocol. The sampling rate was synchronized with the tensile tester controlled by a microcontroller (Arduino Due, Arduino). For the cyclic strain test, the sample was clamped on a universal testing machine (34SC-1, Instron) and went through cyclic strain sequences (10,000 cycles, $\epsilon = 0.5$, 1.38 Hz).

Assembly of LMMNs and circuit components
To connect the LMMN films to external power sources or microcontrollers, copper wires were placed at the ends of the patterns and connected using either silver pastes or small drops of EGaIn. EGaIn was used to secure electrical connections in places where the deformation is large, while the use of silver pastes was limited to locations where external strain is negligible. In order to connect surface-mountable chips and MCUs to the skin-attachable circuit boards made of LMMN, droplets of EGaIn were placed first on the circuits. Microchips were then mounted on the LMNN films

and gently pressed to ensure electrical connection (Supplementary Fig. 24). The interconnects were secured with flowable sealants to prevent damage while deformed.

Demonstration of skin-mountable circuit boards

A skin-mountable circuit board was fabricated with a total thickness of approximately 50 μm. A microcontroller unit (MCU) (ATtiny85, Atmel) was embedded to control three surface-mounted chip LEDs by the touch on a tactile sensor. The tactile sensor is made of an LMMN film and patterned as a rectangular pad to sense capacitance change when touched. The microcontroller was programmed using Arduino software. The LMMN film was also patterned as electrical wires to connect the components to an external power source. After assembling the components and sealing them with the enclosing PDMS layer, the circuit was released from the silicon wafer in water. The circuit was then attached to a human wrist using adhesive silicone. After mounting the circuit on the wrist, the circuit was connected to an external power supply with an input voltage of 3.3 V.

Demonstration of a robotic hand

For the demonstration of teleoperation of a robotic hand (Allegro Hand, Wonik Robotics), serpentine LMMN film (Supplementary Fig. 20) was attached to finger joints (proximal interphalangeal (PIP) joints and metacarpophalangeal (MCP) joints). The resistance data was collected by ADC (ADS1118, Texas Instruments) at a sampling rate of 500 Hz, and transferred to a microcontroller (Arduino Mega 2560, Arduino) via serial peripheral interface (SPI) communication. The finger joint sensor was characterized by a vision camera (Depth Camera D435i, Intel RealSense) based motion detection system (Supplementary Fig. 20). The overall control loop frequency of the integrated teleoperation robotic system was 78.5 Hz.

Demonstration as an energy harvester

Voltages generated based on tribotronics were measured using an oscilloscope (Tektronix, DPO5104B) with a voltage probe (Tektronix, TPP0850, 40 MΩ). A pushing tester (Labworks, LW139.138-40) was used to provide a consistent contact frequency (4 Hz) and a gap distance (20 mm). A grounded aluminum film as a contact material was fixed at a tip of the pushing tester using a VHB double-sided tape. Patterned LMMN film functioning as a TENG was placed on top of the hand for the demonstration of lighting up LEDs by a simple touch. Acrylic-based tape (VHB, 3 M) was placed between the LMMN film and hand, and the pattern was contacted by nitrile gloves to light up 11 serially connected LEDs (Supplementary Movie 2). Both measurements and demonstration were conducted at room temperature after about 1000 pre-contacts to secure stable power generation.

REFERENCES

1. Cianchetti, M., Laschi, C., Menciassi, A. & Dario, P. Biomedical applications of soft robotics. *Nat. Rev. Mater.* **3**, 143–153 (2018).
2. Yu, Y. et al. Biofuel-powered soft electronic skin with multiplexed and wireless sensing for human-machine interfaces. *Sci. Robot.* **5**, eaaz7946 (2020).
3. Park, Y.-L. et al. Design and control of a bio-inspired soft wearable robotic device for ankle-foot rehabilitation. *Bioinsp. Biomim.* **9**, 016007 (2014).
4. Wirekoh, J., Parody, N., Riviere, C. & Park, Y.-L. Design of fiber-reinforced soft bending artificial muscles for wearable tremor suppression devices. *Smart Mater. Struct.* **30**, 015013 (2020).
5. Rus, D. & Tolley, M. T. Design, fabrication and control of soft robots. *Nature* **521**, 467–475 (2015).
6. Majidi, C. Soft robotics: A perspective—current trends and prospects for the future. *Soft Robot* **1**, 5 (2014).
7. Shin, H.-S. et al. Bio-inspired large-area soft sensing skins to measure UAV wing deformation in flight. *Adv. Funct. Mater.* **31**, 2100697 (2021).
8. Kwon, J. et al. Selectively stiffening garments enabled by cellular composites. *Adv. Mater. Technol.* 2101543, https://doi.org/10.1002/admt.202101543 (2022).
9. Kim, T. et al. Heterogeneous sensing in a multifunctional soft sensor for human-robot interfaces. *Sci. Robot.* **5**, eabc6878 (2020).
10. Biswas, S., Shao, Y., Hachisu, T., Nguyen-Dang, T. & Visell, Y. Integrated soft opto-electronics for wearable health monitoring. *Adv. Mater. Technol.* **5**, 2000347 (2020).
11. Mengüç, Y. et al. Wearable soft sensing suit for human gait measurement. *Int. J. Robot. Res.* **33**, 1748–1764 (2014).
12. Charalambides, A. & Bergbreiter, S. Rapid manufacturing of mechanoreceptive skins for slip detection in robotic grasping. *Adv. Mater. Technol.* **2**, 1600188 (2017).
13. Shin, G., Lee, S. & Park, Y.-L. Selective patterning of conductive elastomers embedded with silver powders and carbon nanotubes for stretchable electronics. *IEEE Robot. Autom. Lett.* **7**, 4983–4990 (2022).
14. Shih, B. et al. Electronic skins and machine learning for intelligent soft robots. *Sci. Robot.* **5**, eaaz9239 (2020).
15. Liu, Y., Pharr, M. & Salvatore, G. A. Lab-on-skin: A review of flexible and stretchable electronics for wearable health monitoring. *ACS Nano* **11**, 9614–9635 (2017).
16. Wang, S., Oh, J. Y., Xu, J., Tran, H. & Bao, Z. Skin-inspired electronics: An emerging paradigm. *Acc. Chem. Res.* **51**, 1033–1045 (2018).
17. Kim, D., Kwon, J., Han, S., Park, Y.-L. & Jo, S. Deep full-body motion network (DFM-Net) for a soft wearable motion sensing suit. *IEEE/ASME Trans. Mechatron.* **24**, 56–66 (2019).
18. Li, B., Shi, Y., Hu, H., Fontecchio, A. & Vissel, Y. Assemblies of microfluidic channels and micropillars facilitate sensitive and compliant tactile sensing. *IEEE Sens. J.* **16**, 8908–8915 (2016).
19. Someya, T., Bao, Z. & Malliaras, G. G. The rise of plastic bioelectronics. *Nature* **540**, 379–385 (2016).
20. Kim, D.-H. et al. Materials and noncoplanar mesh designs for integrated circuits with linear elastic responses to extreme mechanical deformations. *Proc. Natl Acad. Sci. USA* **105**, 18675–18680 (2008).
21. Webb, R. C. et al. Ultrathin conformal devices for precise and continuous thermal characterization of human skin. *Nat. Mater.* **12**, 938–944 (2013).
22. Kaltenbrunner, M. et al. Ultrathin and lightweight organic solar cells with high flexibility. *Nat. Commun.* **3**, 770 (2012).
23. Kang, D. et al. Ultrasensitive mechanical crack-based sensor inspired by the spider sensory system. *Nature* **516**, 222–226 (2014).
24. Kim, D.-H. et al. Epidermal electronics. *Science* **333**, 838–843 (2011).
25. Kaltenbrunner, M. et al. An ultra-lightweight design for imperceptible plastic electronics. *Nature* **499**, 458–463 (2013).
26. Choi, S., Han, S. I., Kim, D., Hyeon, T. & Kim, D.-H. High-performance stretchable conductive nanocomposites: materials, processes, and device applications. *Chem. Soc. Rev.* **48**, 1566–1595 (2019).
27. Fu, S. et al. Fabrication of large-area bimodal sensors by all-inkjet-printing. *Adv. Mater. Technol.* **4**, 1800703 (2019).
28. Kim, J. et al. Simultaneous monitoring of sweat and interstitial fluid using a single wearable biosensor platform. *Adv. Sci.* **5**, 1800880 (2018).
29. Cui, Z., Han, Y., Huang, Q., Dong, J. & Zhu, Y. Electrohydrodynamic printing of silver nanowires for flexible and stretchable electronics. *Nanoscale* **10**, 6806–6811 (2018).
30. Wang, S. et al. Skin electronics from scalable fabrication of an intrinsically stretchable transistor array. *Nature* **555**, 83–88 (2018).
31. Gu, J. et al. Self-powered strain sensor based on the piezo-transmittance of a mechanical metamaterial. *Nano Energy* **89**, 106447 (2021).
32. Kim, B. H. et al. High-resolution patterns of quantum dots formed by electro-hydrodynamic jet printing for light-emitting diodes. *Nano Lett.* **15**, 969–973 (2015).
33. To, C., Hellebrekers, T. L., Jung, J., Yoon, S. J. & Park, Y.-L. A soft optical waveguide coupled with fiber optics for dynamic pressure and strain sensing. *IEEE Robot. Autom. Lett.* **3**, 3216–3223 (2018).
34. Kim, S. Y. et al. Sustainable manufacturing of sensors onto soft systems using self-coagulating conductive Pickering emulsions. *Sci. Robot.* **5**, eaay3604 (2020).
35. Hong, S. et al. Stretchable electrode based on laterally combed carbon nanotubes for wearable energy harvesting and storage devices. *Adv. Funct. Mater.* **27**, 1704353 (2017).

36. Dickey, M. D. Stretchable and soft electronics using liquid metals. *Adv. Mater.* **29**, 1606425 (2017).
37. Dickey, M. D. et al. Eutectic gallium-indium (EGaln): A liquid metal alloy for the formation of stable structures in microchannels at room temperature. *Adv. Funct. Mater.* **18**, 1097–1104 (2008).
38. Kim, K. et al. Highly sensitive and wearable liquid metal-based pressure sensor for health monitoring applications: Integration of a 3D-printed microbump array with the microchannel. *Adv. Healthc. Mater.* **8**, 1900978 (2019).
39. Park, Y.-L., Chen, B.-r. & Wood, R. J. Design and fabrication of soft artificial skin using embedded microchannels and liquid conductors. *IEEE Sens. J.* **12**, 2711–2718 (2012).
40. Do, T. N. & Visell, Y. Stretchable, twisted conductive microtubules for wearable computing, robotics, electronics, and healthcare. *Sci. Rep.* **7**, 1753 (2017).
41. Boley, J. W., White, E. L., Chiu, G. T.-C. & Kramer, R. K. Direct writing of gallium-indium alloy for stretchable electronics. *Adv. Funct. Mater.* **24**, 3501–3507 (2014).
42. Shin, G., Jeon, B. & Park, Y.-L. Direct printing of sub-30 µm liquid metal patterns on three-dimensional surfaces for stretchable electronics. *J. Micromech. Microeng.* **30**, 034001 (2020).
43. Hirsch, A., Dejace, L., Michaud, H. O. & Lacour, S. P. Harnessing the rheological properties of liquid metals to shape soft electronic conductors for wearable applications. *Acc. Chem. Res.* **52**, 534–544 (2019).
44. Kim, M. S. et al. Stretchable printed circuit board based on leak-free liquid metal interconnection and local strain control. *ACS Appl. Mater. Interfaces* **14**, 1826–1837 (2022).
45. Hirsch, A. & Lacour, S. P. A method to form smooth films of liquid metal supported by elastomeric substrate. *Adv. Sci.* **5**, 1800256 (2018).
46. Dejace, L., Laubeuf, N., Furfaro, I. & Lacour, S. P. Gallium-based thin films for wearable human motion sensors. *Adv. Intell. Syst.* **1**, 1900079 (2019).
47. Li, G., Wu, X. & Lee, D.-W. Selectively plated stretchable liquid metal wires for transparent electronics. *Sens. Actuators B* **221**, 1114–1119 (2015).
48. Hirsch, A., Michaud, H. O., Gerratt, A. P., de Mulatier, S. & Lacour, S. P. Intrinsically stretchable biphasic (solid–liquid) thin metal films. *Adv. Mater.* **28**, 4507–4512 (2016).
49. Kim, M., Kim, C., Alrowais, H. & Brand, O. Multiscale and uniform liquid metal thin-film patterning based on soft lithography for 3D heterogeneous integrated soft microsystems: Additive stamping and subtractive reverse stamping. *Adv. Mater. Technol.* **3**, 1800061 (2018).
50. Pan, C. et al. Visually imperceptible liquid-metal circuits for transparent, stretchable electronics with direct laser writing. *Adv. Mater.* **30**, 1706937 (2018).
51. Kim, M., Brown, D. K. & Brand, O. Nanofabrication for all-soft and high-density electronic devices based on liquid metal. *Nat. Commun.* **11**, 1002 (2020).
52. Dejace, L., Chen, H., Furfaro, I., Schiavone, G. & Lacour, S. P. Microscale liquid metal conductors for stretchable and transparent electronics. *Adv. Mater. Technol.* **6**, 2100690 (2021).
53. Mohammed, M. G. & Kramer, R. All-printed flexible and stretchable electronics. *Adv. Mater.* **29**, 1604965 (2017).
54. Boley, J. W., White, E. L. & Kramer, R. K. Mechanically sintered gallium-indium nanoaparticles. *Adv. Mater.* **29**, 2355–2360 (2015).
55. Liu, S. et al. Laser sintering of liquid metal nanoparticles for scalable manufacturing of soft and flexible electronics. *Acs. Appl. Mater. Interfaces* **10**, 28232–28241 (2018).
56. Ford, M. J., Patel, D. K., Pan, C., Bergbreiter, S. & Majidi, C. Controlled assembly of liquid metal inclusions as a general approach for multifunctional composites. *Adv. Mater.* **32**, 2002929 (2020).
57. Yu, F. et al. Ga-In liquid metal nanoparticles prepared by physical vapor deposition. *Prog. Nat. Sci.: Mater. Int.* **28**, 28–33 (2018).
58. Wang, P.-F. et al. Facile fabrication of eutectic gallium-indium alloy nanostructure and application in photodetection. *Nanotechnology* **31**, 145703 (2020).
59. Bosio, L. & Windsor, C. G. Observation of a metastability limit in liquid gallium. *Phys. Rev. Lett.* **35**, 1652 (1975).
60. Thrasher, C. J., Farrell, Z. J., Morris, N. J., Willey, C. L. & Tabor, C. E. Mechanoresponsive polymerized liquid metal networks. *Adv. Mater.* **31**, 1903864 (2019).
61. Tian, K. et al. 3D printing of transparent and conductive heterogeneous hydrogel–elastomer systems. *Adv. Mater.* **29**, 1604827 (2017).
62. Zhao, Y., Khandagale, P. & Majidi, C. Modeling electromechanical coupling of liquid metal embedded elastomers while accounting stochasticity in 3D percolation. *Extrem. Mech. Lett.* **48**, 101443 (2021).
63. Tang, L., Mou, L., Zhang, W. & Jiang, X. Large-scale fabrication of highly elastic conductors on a broad range of surfaces. *ACS Appl. Mater. Interfaces* **11**, 7138–7147 (2019).
64. Yamada, T. et al. A stretchable carbon nanotube strain sensor for human-motion detection. *Nat. Nanotechnol.* **6**, 296–301 (2011).
65. Ling, Y. et al. Disruptive, soft, wearable sensors. *Adv. Mater.* **32**, 1904664 (2019).
66. Lee, Y., Cha, S. H., Kim, Y.-W., Choi, D. & Sun, J.-Y. Transparent and attachable ionic communicators based on self-cleanable triboelectric nanogenerators. *Nat. Commun.* **9**, 1804 (2018).
67. Lee, Y., Song, W. J. & Sun, J.-Y. Hydrogel soft robotics. *Mater. Today Phys.* **15**, 100258 (2020).

ACKNOWLEDGEMENTS

AUTHOR CONTRIBUTIONS

Y.P. and J.J. contributed equally to this work. Y.P. and J.J. conceived the idea, carried out the experiments, analyzed the data, performed demonstration and wrote the main manuscript text. Y.L. provided advice on developing triboelectric nanogenerators and wrote the manuscript. Y.-L.P. supervised this study and provided intellectual and technical guidance. D.L. and J.J.V. reviewed and commented on the manuscript. All authors discussed the results and commented on the manuscript.

COMPETING INTERESTS

Y.P., J.J., and Y.-L.P. are included in a Korea patent application that covers the LBL deposition process and the fabrication of LMMN films, which has been submitted by the SNU R&DB Foundation. The other authors declare no competing interests.

ADDITIONAL INFORMATION

Supplementary information The online version contains supplementary material available at https://doi.org/10.1038/s41528-022-00215-2.

Correspondence and requests for materials should be addressed to Yong-Lae Park.

Reprints and permission information is available at http://www.nature.com/reprints

Publisher's note Springer Nature remains neutral with regard to jurisdictional claims in published maps and institutional affiliations.